



The effect of manganese vacancy in birnessite-type MnO_2 on room-temperature oxidation of formaldehyde in air

Jinlong Wang^a, Jinge Li^a, Chuanjia Jiang^b, Peng Zhou^b, Pengyi Zhang^{a,*}, Jiaguo Yu^{b,**}

^a State Key Joint Laboratory of Environment Simulation and Pollution Control, School of Environment, Tsinghua University, Beijing 100084, China

^b State Key Laboratory of Advance Technology for Material Synthesis and Processing, Wuhan University of Technology, Wuhan 430070, China



ARTICLE INFO

Article history:

Received 11 August 2016

Received in revised form 18 October 2016

Accepted 17 November 2016

Available online 17 November 2016

Keywords:

Birnessite-type MnO_2

Manganese vacancy

Formaldehyde

Indoor air

Catalysis

ABSTRACT

Catalytic reaction active site tends to be the structural defects, such as edges, corners, ribs and other position that has low coordination number. Here, the potassium (K^+) type birnessite (i.e. a layered-structure MnO_2) was designed with different amounts of manganese vacancy (V_{Mn}) for catalytic oxidation of formaldehyde (HCHO). The content of V_{Mn} was determined by the ratio of Mn/O and coordination number of Mn–Mn edge-sharing structure. The V_{Mn} showed a dramatic promotion effect on the activity of birnessite for HCHO oxidation. The specific rate at 30 °C over the birnessite with the highest content of V_{Mn} was highest (0.052 $\mu\text{mol}/\text{m}^2 \text{min}$) under 40 ppm of HCHO, 120,000 mL/g h of GHSV and ~80% of relative humidity. The presence of V_{Mn} induced unsaturated oxygen species and K^+ locating nearby V_{Mn} sites for charge balance facilitated the formation of active oxygen species, accordingly the activity for HCHO oxidation was greatly improved. This finding reveals a way to enhance the catalytic activity of metal oxides via adjusting metal vacancies.

© 2016 Elsevier B.V. All rights reserved.

1. Introduction

Formaldehyde (HCHO) is known as one of the most prevalent pollutants in indoor environment. It is mainly released from the continuous release of hydrolysis reaction of urea-formaldehyde resin used in the decorative furniture under a certain temperature and humidity conditions [1]. Long-term exposure to HCHO threatens human health and cause a lot of health problems. Heterogeneous catalysis is one of the most effective methods to remove HCHO. In recent years, room-temperature catalysis has been widely investigated to remove HCHO [2–5]. Supported noble metal catalysts have been reported to decompose HCHO into carbon dioxide and water at low temperature with great efficiency [6–11]. However, their wide application is restricted by the high cost of noble metals.

Birnessite is a kind of layered manganese dioxide (MnO_2) which is built by edge-sharing octahedral MnO_6 . A certain number of water and cations (e.g. Li^+ , Na^+ , K^+ , Ca^{2+}) are located in the layers for charge balance. MnO_2 has recently emerged as prospective materials for a wide and potential applications in water oxidation, energy storage and pollution abatement [12–14]. Recent work indicates the ability of birnessite to decompose formaldehyde. Zhang

et al. [15] compared the activity of α -, β -, γ - and δ - MnO_2 (i.e. birnessite) and found that the tunneling structure and the active lattice oxygen contribute to the good activity of δ - MnO_2 . He et al. [16] synthesized porous birnessite, which showed good activity for HCHO complete oxidation. Our group recently reported that birnessite exhibited the activity for the complete decomposition of HCHO under room temperatures, and the content of water and interlayer cations had dramatic effect on its activity due to their influence on surface hydroxyl, which acted as active species in formaldehyde oxidation [17–19].

Defect adjustment is regarded an effective method to regulate the surface electronic properties of different catalysts [20]. Active sites on heterogeneous catalysts have long been supposed to be strongly associated with surface defects [21,22]. Oxygen vacancies commonly exist in metal oxides, which act as adsorption and active sites in heterogeneous catalytic reactions [21–23]. Furthermore, the surface adsorption and reactivity of adsorbates such as oxygen or water can be affected by additional electrons around the oxygen vacancy [23]. Recently, hydrogenated TiO_2 was reported to exhibit a HCHO oxidation activity in the dark, which was explained by the introduced oxygen vacancies and surface hydroxyl groups [24]. Xu et al. also reported that the presence of oxygen vacancy on Au/CeO_2 promoted the HCHO oxidation activity [8].

On the other hand, cation vacancy is another important defect. The presence of manganese vacancy (V_{Mn}) in birnessite has been

* Corresponding author.

** Corresponding author.

E-mail addresses: zpy@tsinghua.edu.cn (P. Zhang), jiaguoyu@yahoo.com (J. Yu).

reported and it can be tuned by the degree of oxidation in the process of synthesis [25,26]. Kwon et al. [27,28] reported that the energy gap of electronic states of MnO_2 between occupied and unoccupied is decreased due to the presence of V_{Mn} , leading to the effectively separation of photo induced charge carriers, which enhance the photoconductivity of MnO_2 . Wang et al. [20] found that the introduction of cation vacancy would increase half-metallicity property of the one-layered MnO_2 nanosheet. The spin-down states of the half-metallic gaps decrease from 1.81 eV to 1.23 eV with increasing V_{Mn} concentration from 2.8% to 11.1%. To the best of our knowledge, the effect of cation vacancy on catalytic oxidation has never been reported.

In this work, we prepared birnessite with different contents of V_{Mn} and found that the activity of birnessite for HCHO oxidation was significantly influenced by the content of V_{Mn} . It is proposed that V_{Mn} in birnessite leads to abundant surface adsorbed oxygen. Meanwhile, the presence of potassium ions (K^+) nearby V_{Mn} promoted the activation of surface oxygen species, which enhance the catalytic oxidation activity for HCHO oxidation.

2. Experimental

2.1. Preparation of birnessite with different contents of V_{Mn}

All chemicals used for the preparation were of analytical grade and the water was deionized water. Birnessite samples were synthesized by a facile redox reaction between KMnO_4 and $(\text{NH}_4)_2\text{C}_2\text{O}_4$, during which the content of V_{Mn} was tuned by changing the ratio of KMnO_4 to $(\text{NH}_4)_2\text{C}_2\text{O}_4$. The detailed procedure is as follows. 1.0 g of KMnO_4 and $(\text{NH}_4)_2\text{C}_2\text{O}_4$ H_2O (0.4 g, 0.8 g or 1.8 g) were dissolved in 130 mL of deionized water in a erlenmeyer flask. Then, the erlenmeyer flask was placed in a bath with shaking speed of 150 rpm. The bath temperature was kept at 90 °C for 10 h reaction. After the flask was cooled down, the precipitate was centrifuged and then washed 3 times with deionized water to remove possible residual impurities. The precipitate was dried in an oven at 105 °C for 24 h. The corresponding samples are denoted as $V_{\text{Mn}}\text{-}3$, $V_{\text{Mn}}\text{-}2$ and $V_{\text{Mn}}\text{-}1$.

2.2. Characterization

Scanning electron microscopy (SEM) was recorded on a Merlin field emission scanning electron microscope (Carl Zeiss, Germany) operated at 5 kV. All birnessite samples were coated with carbon to increase their electrical conductivity. Transmission electron microscopy (TEM) was performed on a JEOL 2011 transmission electron microscope (JEOL, Japan) operated at an accelerating voltage of 150 kV. X-ray diffraction (XRD) analysis of birnessite samples were carried out on a D8-Advance X-ray diffractometer (Bruker, Germany) using $\text{Cu K}\alpha$ radiation ($\lambda=0.1542 \text{ nm}$). X-ray photoelectron spectroscopy (XPS) analysis was recorded on a ESCALAB 250Xi X-ray photoelectron spectrometer (Thermo Fisher, USA) operated at a pass energy of 30 eV, using $\text{Al K}\alpha$ ($\lambda=1486.7 \text{ eV}$) as an exciting X-ray source. The spectra were adjusted with respect to the C 1 s line of adventitious carbon at 284.8 eV. Nitrogen adsorption-desorption experiments were conducted on an Autosorb-1MP automated surface and pore size analyzer (Quantachrome, USA). The specific surface area was calculated by a multipoint Brunauer-Emmett-Teller (BET) method using adsorption data in a relative pressure (P/P_0) range of 0.05–0.25. The pore volume was obtained at the relative pressure(P/P_0) of 0.99. Before the measurement, the catalysts were degassed in vacuum at 200 °C for 4 h. The X-ray Absorption Spectroscopy (XAS) of the different birnessite samples and reference materials ($\beta\text{-MnO}_2$ and $\alpha\text{-Mn}_2\text{O}_3$) were measured at Beijing Synchrotron Radiation Facility (BSRF). The average oxidation state

(AOS) of different birnessite-type MnO_2 was detected by their position of near-edge X-ray absorption. For comparison, MnO , Mn_3O_4 , Mn_2O_3 and MnO_2 with definite Mn oxidation states were used as standard. The extended X-ray Absorption Fine Structure (EXAFS) data were conducted using IFEFFIT as reported. For Mn K -edge, $E_0 = 6559 \text{ eV}$, $R_{\text{bkg}} = 0.9 \text{ \AA}$ and $k\text{-weight} = 3$. Structural parameters were acquired by fitting the experimental k^3 -weighted EXAFS spectra to the standard one. Data reduction steps were performed using IFEFFIT program. Amplitude attenuation factor (S_0^{-2}), Debye-Waller factor (σ^2), changes of interatomic distance (Δr) and changes of energy (ΔE_0) which were all relaxed at first and set as 1, 0.003, 0 and 0 before simulation, respectively. The coordination number of $\text{Mn}^{4+}\text{-Mn}^{4+}$ and $\text{Mn}^{3+}\text{-Mn}^{4+}$ was calculated by $CN(6) \times S_0^{-2}$. After the fitting, the result will be decided by R factor (<0.02) and chi-square (>10).

Hydrogen temperature programmed reduction ($\text{H}_2\text{-TPR}$) was conducted on an AutoChem 2920 adsorption apparatus (Micromeritics, USA) equipped with a TCD detector. In a typical experiment, 50 mg catalyst was loaded in and pretreated with He (50 mL/min) at 150 °C for 1 h. After cooling down to room temperature, the analysis gas was changed to H_2 (5% H_2/Ar) with a flow rate of 60 mL/min and the temperature was then programmed to rise at a ramp of 5 °C/min up to 500 °C. In situ diffuse reflectance infrared Fourier transform spectroscopy (In situ DRIFTS) was performed on a NICOLET 6700 FTIR spectrometer (Micromeritics, USA) with an in situ cell to clarify the intermediate species during HCHO oxidation and its mechanism. All spectra were recorded with a resolution of 4 cm^{-1} and an accumulation of 32 scans. Samples were pretreated by N_2 for 30 min under room temperature before exposed to HCHO containing gas phase. Then, HCHO (~80 ppm) was injected into the cell at a flow rate of 30 mL/min with the pressured oxygen as the balance gas.

2.3. Evaluation of HCHO removal activity

The evaluation of the catalytic activity system includes two parts: static and dynamic experiment.

As for static experiment, the catalytic activity of different birnessite samples were evaluated in an organic glass reactor covered by a layer of aluminum foil on its inner wall. The temperature inside the reactor was maintained at 25 °C during the reaction process. The relative humidity (RH) was not controlled inside the reactor, which was close to the indoor environment. The RH was about 60% for static experiment. The concentration of HCHO and CO_2 were analyzed online with a Photoacoustic IR Multigas Monitor (INNOVA air Tech Instruments Model 1412). Typically, 50 mg of sample was placed on the bottom of a glass Petri dish. After placing the sample-containing dish at the bottom of reactor with a glass slide cover, 3.7 μL of HCHO (38%) solution was injected into the reactor. After the HCHO was volatilized completely and the initial concentration of HCHO was about 150 ppm, the glass cover of the Petri dish was removed to start the catalytic oxidation of HCHO.

As for dynamic experiment, HCHO removal efficiency on different birnessite samples was investigated in a fixed bed flow reactor which was similar to the reference [29]. 100 mg catalyst with 40/60 meshes were loaded in a quartz tube reactor. Humidity was induced in the reaction atmosphere to simulate the real environment condition. The gas steam with relative humidity (~80%) was generated by bubbling air into the water. The inlet concentration of HCHO was set around ~40 ppm by vaporizing the paraformaldehyde. The total flow rate was 200 mL/min. The reaction was conducted from 30 °C to 140 °C. The inlet gas tube was heated to 120 °C to prevent the condensation of the feed gas in the reactor system. The HCHO conversion was estimated according to its final generation of CO_2 . The generation of CO_2 was recorded after 1 h reaction at a certain temperature. The outlet concentration of CO_2 was determined by

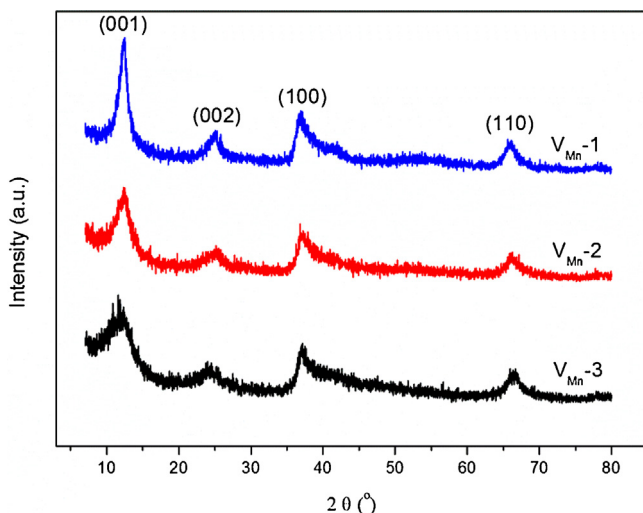


Fig. 1. XRD patterns of birnessite samples prepared with different molar ratios of $\text{KMnO}_4/(\text{NH}_4)_2\text{C}_2\text{O}_4$.

a GC-2014 gas chromatograph (Shimadzu, Japan) equipped with a methanizer and a flame ionization detector (FID).

The specific rate (R) was calculated from dynamic experiment:

$$R \left(\mu\text{mol}/\text{m}^2 \cdot \text{min} \right) = \frac{C_{\text{HCHO}} \div 22.4 \times F \times \eta}{S_{\text{BET}} \times m} \times 10^{-5}$$

where R is the specific rate, C_{HCHO} is the inlet HCHO concentration (ppm), F is the flow rate (mL/min), η is the HCHO conversion calculated by the generation of CO_2 (%), S_{BET} is the specific surface area of the sample and m is the sample weight. To calculate the apparent activation energy (E_a), the conversion of formaldehyde was controlled under 15% and the corresponding GHSV was varied from 60,000 to 240,000 mL/g.h.

3. Results and discussion

3.1. Crystal structure and textural properties

The crystal structure of three samples was detected by XRD measurement (Fig. 1). The intense diffraction peaks of 2θ located around 12.3° (001), 24.6° (002), 36.5° (100) and 65.5° (110) can be assigned to the birnessite structure of hexagonal phase (JCPDS No. 80-1098) with poor crystallinity. Three samples had similar diffraction patterns, however, the intensity of the diffraction peak along (001) facet decreased with the increasing molar ratio of $\text{KMnO}_4/(\text{NH}_4)_2\text{C}_2\text{O}_4$. Besides, the wider peak width of $V_{\text{Mn}-3}$ also implies its poor crystallinity, which may be due to the damage of ordered structure [30].

The morphologies and the structures of different samples were observed by FE-SEM, TEM and HRTEM. FE-SEM and TEM images are shown in Fig. 2a–f. When the molar ratio of $\text{KMnO}_4/(\text{NH}_4)_2\text{C}_2\text{O}_4$ was as low as 0.50 ($V_{\text{Mn}-1}$), flower-like nanospheres consisting of nanosheets formed. When the molar ratio increased, the surface of the nanospheres became denser and the flower-like structure disappeared, while the compact nanospheres formed in sample $V_{\text{Mn}-3}$. Besides, the size of nanoparticles increased from 150 nm to 400 nm with increase in the molar ratio of $\text{KMnO}_4/(\text{NH}_4)_2\text{C}_2\text{O}_4$, which can be ascribed to the formation of smaller amounts of crystal nucleus with lower concentration of $(\text{NH}_4)_2\text{C}_2\text{O}_4$. The high-resolution TEM (HRTEM) images are shown in Fig. 2g–i, the lattice fringes of 3.5\AA and 2.3\AA correspond to the {002} and {100} lattice planes of birnessite. The HRTEM image demonstrated that $V_{\text{Mn}-1}$ showed well-crystallized structure. However, as for $V_{\text{Mn}-2}$ (dashed square in Fig. 2h) and $V_{\text{Mn}-3}$ samples, the reduction in the long-range order

occurred, implying that there was a damage in the crystal structure which was consistent with XRD data. The BET surface area of $V_{\text{Mn}-1}$, $V_{\text{Mn}-2}$ and $V_{\text{Mn}-3}$ is 146.7 , 35.3 and $14.4\text{ m}^2/\text{g}$, respectively. The specific surface area and pore volume data (Table 1) from N_2 adsorption-desorption isotherms were consistent with the information from the SEM/TEM images.

Energy dispersive spectra (EDS) was used to reveal the ratio of Mn and O in different samples (Table 1). The Mn/O molar ratios of $V_{\text{Mn}-1}$, $V_{\text{Mn}-2}$ and $V_{\text{Mn}-3}$ are $0.98:2$, $0.95:2$ and $0.91:2$, respectively, which are slightly below of MnO_2 (1:2) stoichiometric ratio, indicating the presence of V_{Mn} . Wang et al. [20] also used this method to confirm the presence of V_{Mn} in layered manganese dioxides. The presence of V_{Mn} in $[\text{MnO}_6]$ sheets of MnO_2 compounds breaks down the crystal symmetry, leading to the reduction of the crystallinity in the long-range order. As for the XRD analysis, the weaker and wider peak of $V_{\text{Mn}-3}$ may be due to the damage of ordered structure caused by manganese vacancy. Lee et al. [30] also reported similar result in $\text{Na}_{0.44}\text{MnO}_2$ nanowire catalyst, the acid treatment caused the dissolution of Mn^{2+} , leading to the lattice contraction. The average oxidation state as well as the content of H_2O and K^+ were also determined. As shown in Table 1, the average oxidation state (chemical titration method [31]) of $V_{\text{Mn}-1}$, $V_{\text{Mn}-2}$ and $V_{\text{Mn}-3}$ was 3.84 , 3.93 and 3.95 , respectively. In addition, the position of near-edge X-ray absorption energies are dependent on the manganese oxidation state [32]. The Mn K-edge X-ray absorption of four standard manganese oxides (MnO_2 , Mn_2O_3 , Mn_3O_4 and MnO) and different birnessite-type MnO_2 are shown in Fig. S1. The absorption edge in the as-prepared birnessite samples located between that of the Mn_2O_3 and MnO_2 standards, confirming the average oxidation state of Mn in birnessite to be between +3 and +4. A standard calibration curve based on the absorption edge energy was established in order to estimate the average oxidation state of birnessite-type MnO_2 (inset of Fig. S1). As it was calculated, the average oxidation state in $V_{\text{Mn}-1}$, $V_{\text{Mn}-2}$ and $V_{\text{Mn}-3}$ was 3.75 , 3.84 and 3.92 , respectively, which agrees well with the results of chemical titration method. TG analysis was conducted to evaluate the content of water existed in birnessite (Fig. S2). As reported in our previous work, weakly physisorbed water, interlayer water and hydroxyl groups will be desorbed from the birnessite with the rise of temperature accordingly [19]. Weakly physisorbed water and interlayer water usually desorbed below 300°C , which were used to estimate the content of water in birnessite. The water content in $V_{\text{Mn}-1}$, $V_{\text{Mn}-2}$ and $V_{\text{Mn}-3}$ were 13.5% , 14.1% and 13.8% , respectively. Herein, the amount of O was fixed as “2” and to calibrate the content of V_{Mn} , and the chemical formulations of the birnessite are shown in Table 1.

To further learn the structure of different birnessite samples, EXAFS was determined to give quantitative structural information on the atom levels. Coordination number (CN), interatomic distance and the Debye-Waller factor (σ^2) were all provided. In the present study, the Fourier transformed EXAFS data were collected and fitted (Fig. 3). Birnessite is a kind of layered manganese oxides built by edging-sharing $[\text{MnO}_6]$ octahedral, as for this structure, two typical strong Fourier transformed peaks could be observed, which were located at $R + \Delta R$ of ~ 1.5 and 2.5\AA , attributing to Mn-O pairs (the six coordinated oxygen atoms of the nearest neighboring atom around manganese atom) and Mn-Mn pairs (six coordinated manganese atom edge sharing through oxygen atom within $[\text{MnO}_6]$ octahedral slab), respectively (inset of Fig. 3) [12,33,34]. The standard $k^3 \chi(k)$ EXAFS data of all samples were performed in Fig. 4. In addition, EXAFS structural parameters were also listed in Table 2. In our case, the distance between the absorber and backscatter corresponds to the position of the FT peak plus about 0.3 – 0.4\AA . Most of the Mn-O distances are found to be close to 1.9\AA , which is a typical value for $[\text{Mn}^{4+}\text{O}_6]$ octahedra presented as in the reference material $\beta\text{-MnO}_2$. However, there are about 20% of the Mn-O

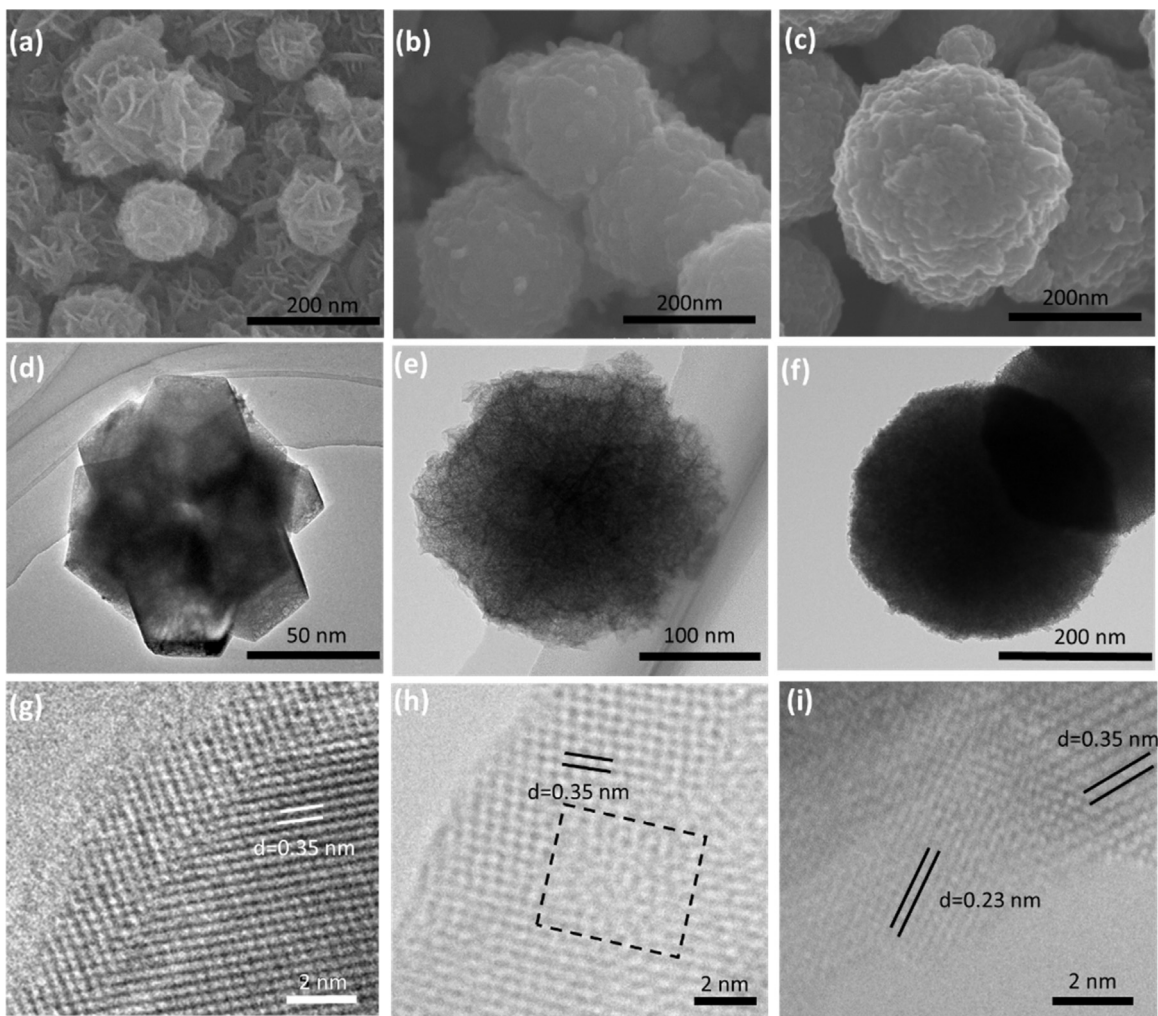


Fig. 2. FESEM, TEM and HRTEM images of different birnessite samples: (a, d, g) V_{Mn}-1, (b, e, g) V_{Mn}-2, (c, f, i) V_{Mn}-3.

distances which are significantly longer (2.3 Å), indicating the contributions of Mn³⁺-O distance (e.g., in α -Mn₂O₃ with two elongated Mn-O distances due to the Jahn-Teller distortion) [12]. As for the second peak, the longer Mn-Mn distances varied due to the localization of layer distortion on the Mn³⁺-rich rows. The Mn-Mn distances in these directions varied periodically between 3.00 Å (Mn³⁺-Mn⁴⁺ pairs) and 2.90 Å (Mn⁴⁺-Mn⁴⁺ pairs), respectively [12]. The second shell was fitted to the Fourier-filtered. The total coordination number of the second peak was six, which can be fitted by Mn⁴⁺-Mn⁴⁺ and Mn⁴⁺-Mn³⁺ pairs.

The coordination of the second Mn-Mn shell is 5.9, close to 6, which means very few V_{Mn} exists in V_{Mn}-1 sample. As for V_{Mn}-3

sample, the total coordination number decreased to 4.9, which indicated increased content of V_{Mn}. Further, the coordination number of Mn⁴⁺-Mn⁴⁺ was almost unchanged (around 3.8), which implied the content of Mn³⁺ decreased from V_{Mn}-1 to V_{Mn}-3. Besides, there was an obvious third peak around 2.9 Å, the distance could be regarded as out-of-layer Mn⁴⁺/Mn³⁺ ions involved in Mn⁴⁺₄(O)₄ cubane formation rather than corner-sharing structure reported in the literature [12]. The peak located around 3.4 Å possibly represents the [MnO₆]⁻K, but here it could not be resolved without suitable reference. The peak located around 5.8 Å (equal to two Mn-Mn distances of 2.88 Å) corresponded to the longer Mn-Mn

Table 1
Properties of different synthesized birnessite catalysts.

Sample	Ratio of KMnO ₄ to (NH ₄) ₂ C ₂ O ₄	S _{BET} (m ² /g)	Pore volume (cm ³ /g)	Average oxidation state (AOS)	K/Mn		Mn/O		Water content (%) ^b	Chemical Formulation ^c		
					Chemical titration ^a	XANES	ICP	EDS	XPS			
V _{Mn} -1	0.50	146.7	0.204	3.84	3.75	0.22	0.10	0.09	0.98:2	0.97:2	13.5	K _{0.21} Mn ³⁺ _{0.15} Mn ⁴⁺ _{0.83} □ _{0.02} O ₂ ·1.13H ₂ O
V _{Mn} -2	1.13	35.3	0.087	3.93	3.84	0.33	0.19	0.25	0.95:2	0.93:2	14.1	K _{0.31} Mn ³⁺ _{0.07} Mn ⁴⁺ _{0.87} □ _{0.06} O ₂ ·1.21H ₂ O
V _{Mn} -3	2.25	14.4	0.056	3.95	3.92	0.39	0.31	0.29	0.91:2	0.89:2	13.8	K _{0.36} Mn ³⁺ _{0.04} Mn ⁴⁺ _{0.88} □ _{0.08} O ₂ ·1.18H ₂ O

^a The average oxidation state of Mn was determined by standard titration using sodium oxalate.

^b The recorded weight loss up to 300 °C was assumed to the elimination of water from the materials.

^c The chemical formulation was gained according to element analysis (ICP), chemical titration and thermogravimetric analysis; □ means Mn vacancy (V_{Mn}).

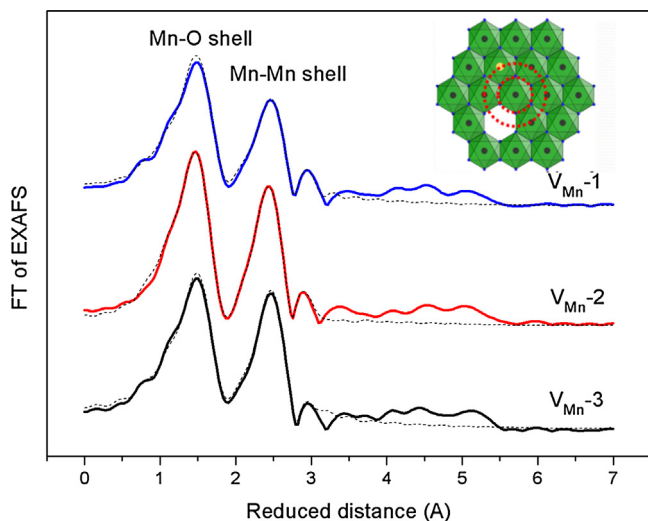


Fig. 3. Fourier-transformed EXAFS spectra of different samples. Each peak relates to a specific structural motif that is schematically depicted (O in red, Mn^{4+} and Mn^{3+} in light and dark purple, respectively). Dashed lines are fitted curve. Top view of the crystal structure of birnessite is shown in the inset (K^+ and H_2O are all relaxed). (For interpretation of the references to colour in this figure legend, the reader is referred to the web version of this article.).

shell. However, the quantification of this signal by EXAFS simulation was unreliable due to the low peak amplitude.

XPS measurements were also performed to investigate the surface chemical state. It exhibited two peaks at 642.4 eV and 654.0 eV, which was assigned to $Mn\ 2p_{3/2}$ and $Mn\ 2p_{1/2}$ (Fig. 5a). The binding energy difference of 11.5 eV indicated that the predominant oxidation state of Mn is +4. After the curve-fitting analysis of $Mn\ 2p_{3/2}$, the ratio between Mn^{4+} species (642.9 ± 0.1 eV) and Mn^{3+} species (641.6 ± 0.1 eV) was calculated by their peak areas [19,35]. For the sample of V_{Mn-1} , the ratio of Mn^{3+}/Mn^{4+} was 35%. When the ratio of $KMnO_4$ to $(NH_4)_2C_2O_4$ increased, the Mn^{3+}/Mn^{4+} in the V_{Mn-3} sample decreased to 10%, implying the content of Mn^{3+} decreased with the increase of manganese vacancy.

The content of K in birnessite was also detected by XPS (Table 1). The ratio of K/Mn increased with the increase of manganese vacancy, indicating the content of K^+ ions increases with increase of V_{Mn} , which is in agreement with the results determined by ICP-AES and EDS. It is well known that potassium ions generally locate

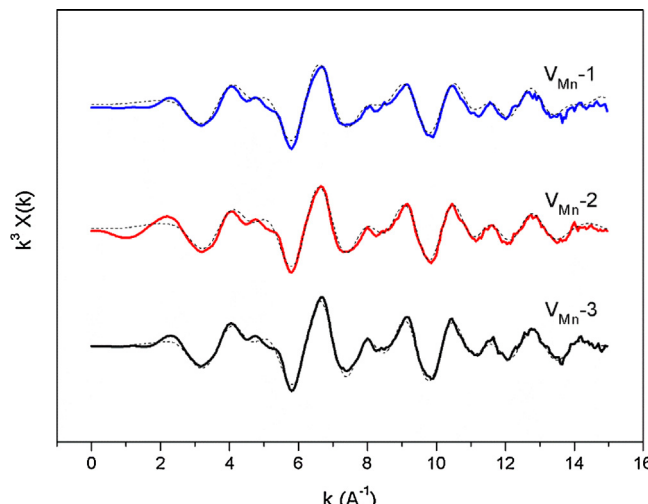


Fig. 4. k^3 -weighted extended-range experimental EXAFS spectra of different birnessite samples and simulation result (black dashed lines).

Table 2

Parameters obtained by simulation of the k^3 -weighted EXAFS spectra (CN, coordination number; R , absorber-backscatter distance; σ^2 , Debye-Waller parameter). The simulated spectra correspond to the Fourier-transformed EXAFS spectra shown in Fig. 3.

	CN	$R(\text{\AA})$	$\sigma^2 (\text{\AA}^2)$
V_{Mn-1} R factor:0.003			
Mn^{4+} -O	3.9	1.89	0.004
Mn^{3+} -O	1.7	2.29	0.011
Mn^{4+} - Mn^{4+} edge sharing	3.8	2.87	0.004
Mn^{3+} - Mn^{4+} edge sharing	2.1	2.98	0.003
Mn_{layer} - $Mn_{interlayer}$	1.0	3.17	0.003
V_{Mn-2} R factor:0.001			
Mn^{4+} -O	4.0	1.90	0.004
Mn^{3+} -O	1.6	2.29	0.011
Mn^{4+} - Mn^{4+} edge sharing	3.7	2.87	0.004
Mn^{3+} - Mn^{4+} edge sharing	1.6	2.97	0.002
Mn_{layer} - $Mn_{interlayer}$	1.1	3.16	0.005
V_{Mn-3} R factor:0.001			
Mn^{4+} -O	4.1	1.90	0.004
Mn^{3+} -O	1.4	2.32	0.011
Mn^{4+} - Mn^{4+} edge sharing	3.7	2.88	0.006
Mn^{3+} - Mn^{4+} edge sharing	1.2	3.00	0.008
Mn_{layer} - $Mn_{interlayer}$	1.4	3.18	0.009

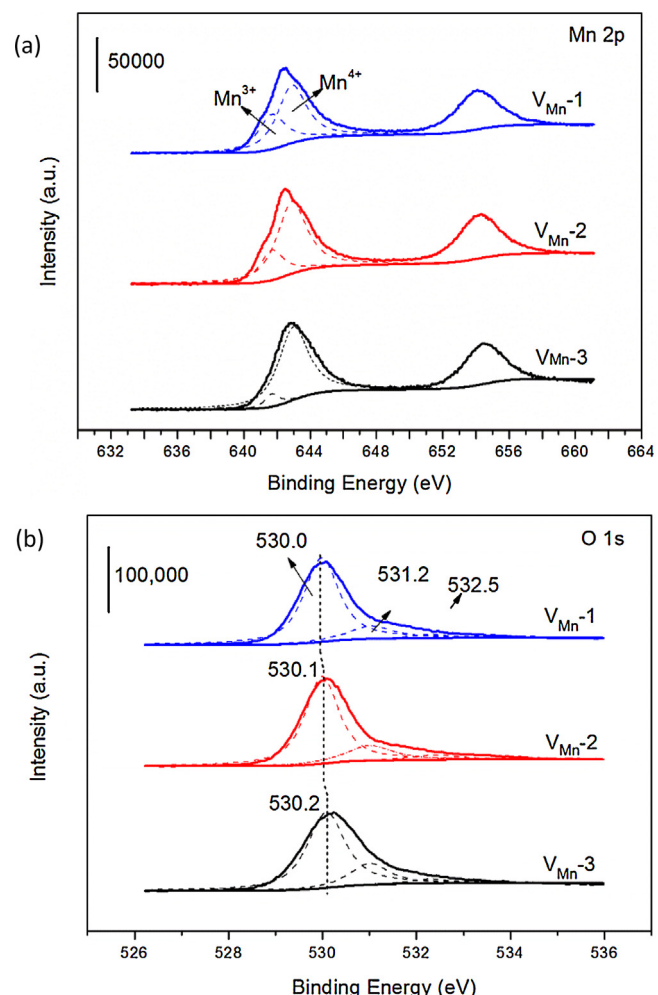


Fig. 5. XPS of $Mn\ 2p$ (a) and $O\ 1s$ (b) of different birnessite samples.

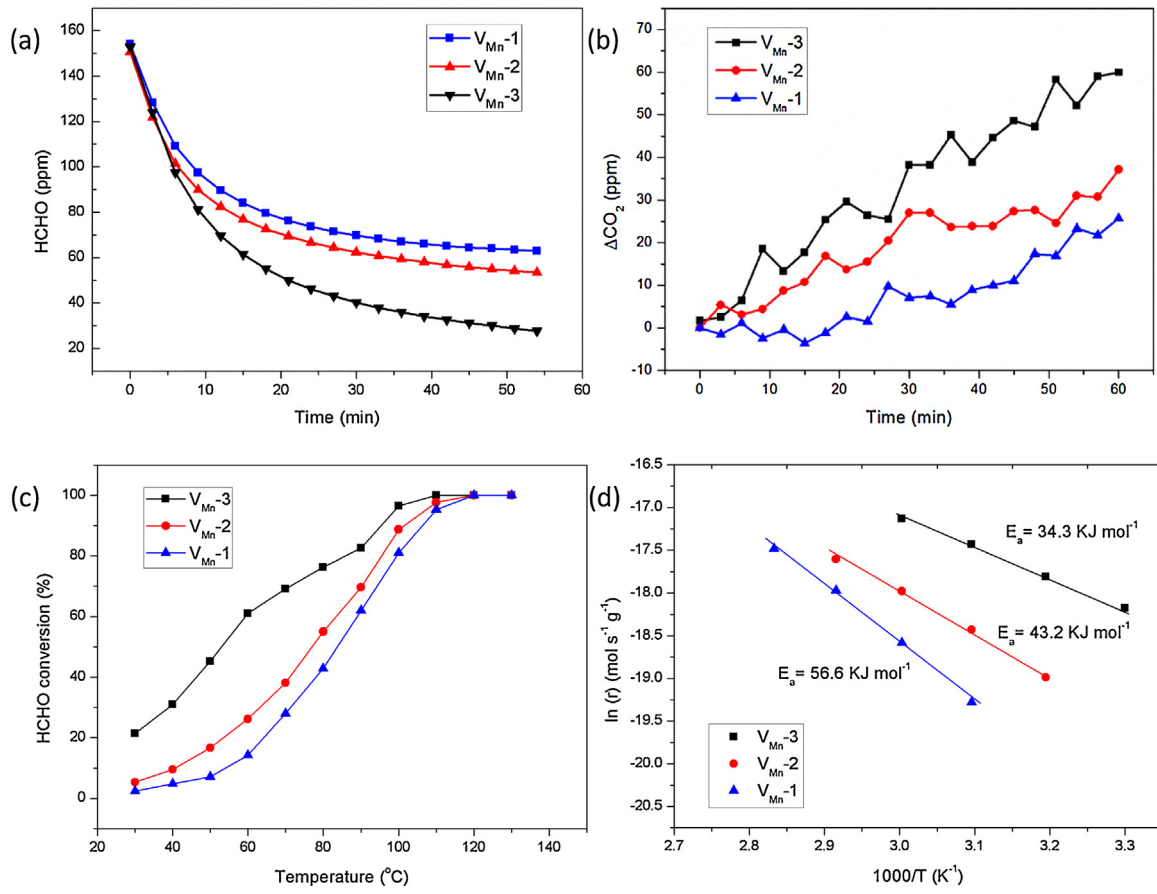


Fig. 6. (a) Changes of HCHO concentration, (b) generation of CO_2 , (c) HCHO conversions with the rise of temperature and (d) Arrhenius plots of the three samples.

between layers to compensate the charge imbalance caused by manganese vacancy. Thus, it is undoubtedly that the content of K^+ increases with the content of V_{Mn} .

The O 1s spectra of different birnessite samples are shown in Fig. 5b. The binding energy at around 529.7–530.3 eV, 531.4–531.8 eV and 532.9–533.7 eV, corresponded to lattice oxygen (O_{latt}) for the tetravalent oxide, surface adsorption oxygen species (O_{ads}) and surface residual water, respectively [19,35]. The binding energy of O_{latt} located at 530.0 eV as for $V_{Mn}-1$, and it shifted to 530.1 and 530.2 eV for $V_{Mn}-2$ and $V_{Mn}-3$, respectively. It can be explained that the electron density around O_{latt} due to Mn vacancy reduces, thus increased the binding energy of lattice oxygen. The ratio of O_{ads}/O_{latt} increased from 20% ($V_{Mn}-1$) to 29% ($V_{Mn}-3$) with the increase of manganese vacancy. This result suggests that $V_{Mn}-3$ has the most abundant surface adsorbed oxygen (such as O_2^- , O^- , and terminal OH group [36,37]). Higher content of terminal OH group also promoted the aggregation of nanoparticles due to the hydrogen bonding interaction, resulting in the increase of particle size and decrease of specific surface area (Table 1). As mentioned above, interlayer K^+ ion increases with V_{Mn} for charge compensation, it has larger ionic radius (K^+ : 1.38 Å, Mn^{4+} : 0.54 Å) [27,28] and low valence, some of oxygen atoms around V_{Mn} still become unsaturated and accordingly hydroxylated. The bond between K^+ and unsaturated oxygen around V_{Mn} is not as strong as the bond Mn-O, thus these unsaturated oxygens are more easily mobile and act as active oxygen species. Fu et al. [38] reported an Au/CeO₂ catalyst for water gas oxidation, in which Au⁺ partially filled the vacant site of Ce and created additional oxygen vacancy. Qiao et al. [39] argued that in the Pt/FeOx catalyst for CO oxidation, single Pt atoms occupied the positions of surface Fe atoms of Fe₂O₃, which lowered the formation energy of oxygen vacancy.

3.2. Performance for HCHO oxidation

The performance of as-synthesized birnessite samples with different V_{Mn} contents for HCHO removal was shown in Fig. 6. As for static experiment (Fig. 6a and b), the HCHO removal ratio within 1 h by $V_{Mn}-1$, $V_{Mn}-2$ and $V_{Mn}-3$ was 59.1%, 67.5% and 81.7%, respectively. Meanwhile, the formation of CO_2 accompanied with HCHO oxidation. Birnessite with higher V_{Mn} content showed higher generation of CO_2 (60, 35 and 21 ppm for $V_{Mn}-3$, $V_{Mn}-2$ and $V_{Mn}-1$, respectively). Therefore, it could be concluded that the activities of the three birnessite samples enhanced in the order of $V_{Mn}-1 < V_{Mn}-2 < V_{Mn}-3$. However, it is still not sufficient enough to use static experiment to evaluate the activity of different birnessite samples. Furthermore, dynamic experiment was also used to investigate the influence of V_{Mn} on the catalytic activity of different birnessite samples (Fig. 6c). T_{50} and T_{90} (corresponding to 50% and 90% HCHO conversion, respectively) were used to evaluate the performance of all three samples. As can be seen in Table 3, the values of T_{50} for $V_{Mn}-1$, $V_{Mn}-2$, and $V_{Mn}-3$ are 84, 77 and 53 °C, meanwhile, T_{90} are 107, 102 and 96 °C, respectively. Water vapor was both introduced in the static and dynamic experiment to simulate the indoor environment. It was reported that water vapor usually had a negative effect on catalytic activity through its competitive adsorption on active site [29]. In our previous work, we found that water vapor also played a positive effect on HCHO oxidation, which will not only facilitate the regeneration of hydroxyl but also promote the desorption of carbonate species by competitive adsorption, however, higher content of water vapor will inhibit the catalytic activity [17].

The effects of the physical adsorption and the specific surface area on HCHO removal were also checked. The specific HCHO

Table 3

HCHO oxidation activity and apparent activation energies (E_a) of the three birnessite samples.

Sample	Catalytic activity (°C)		Rate at 30 °C (μmol/min)	Specific rate at 30 °C (μmol/m² min)	Apparent activation energy (kJ/mol)
	T ₅₀	T ₉₀			
V _{Mn} -1	84	107	0.011	0.001	56.6
V _{Mn} -2	77	102	0.018	0.005	43.2
V _{Mn} -3	53	96	0.075	0.052	34.3

reaction rates (per unit surface area of catalyst) at 30 °C, which was more intrinsic to evaluate the catalytic efficiency of different samples were used. As can be seen from Table 3, the value of specific HCHO reaction rates for V_{Mn}-1, V_{Mn}-2, and V_{Mn}-3 samples were 0.001, 0.005, and 0.052 μmol/m² min, respectively. V_{Mn}-3 showed the highest specific HCHO reaction rates, which was 52.0 and 10.4 times higher than those of V_{Mn}-1 and V_{Mn}-2, respectively. Thus, it can be concluded that the HCHO removal efficiency depends on the content of V_{Mn} rather than the specific surface area. Besides, the apparent activation energy (E_a) was also calculated according to Arrhenius plots for different birnessite samples, which was shown in Fig. 6d. The value of E_a for V_{Mn}-1, V_{Mn}-2, and V_{Mn}-3 samples were 56.6, 43.2, and 34.3 kJ/mol, respectively. As a result, the E_a value of V_{Mn}-3 was lowest among the three samples, indicating HCHO was more easily oxidized on V_{Mn}-3. The HCHO catalytic oxidation of different manganese oxides is listed in Table 4. Under similar reaction conditions, the T_{50%} value (53 °C) in this work is much lower than any other kinds of manganese oxides reported in the literatures. However, efforts should be still made to improve its room temperature catalytic activity for practical use.

3.3. Mechanism of formaldehyde oxidation

To observe the insights into the reaction mechanism of catalytic HCHO oxidation over catalysts with different V_{Mn} contents, the reducibility of as-prepared samples was evaluated by H₂-TPR to differentiate the activity of surface oxygen (Fig. 7). The TPR profile of different birnessite-type MnO₂ was deconvoluted into four peaks, respectively, defined as α, β, γ and δ. Among them, α peak is assigned to the consumption of surface adsorbed oxygen, while β, γ and δ peaks with the peak area ratio of 3:1:2 could be assigned to successive reductions of K_xMnO₂ → Mn₂O₃ → Mn₃O₄ → MnO, respectively. The reduction temperature of α peak for V_{Mn}-1, V_{Mn}-2 and V_{Mn}-3 are 507, 497 and 484 K, respectively. V_{Mn}-3 containing the highest contents of K⁺ and Mn vacancy exhibited the lowest onset reduction temperature among all samples, indicating that surface oxygen associated with K⁺-V_{Mn} ions becomes more

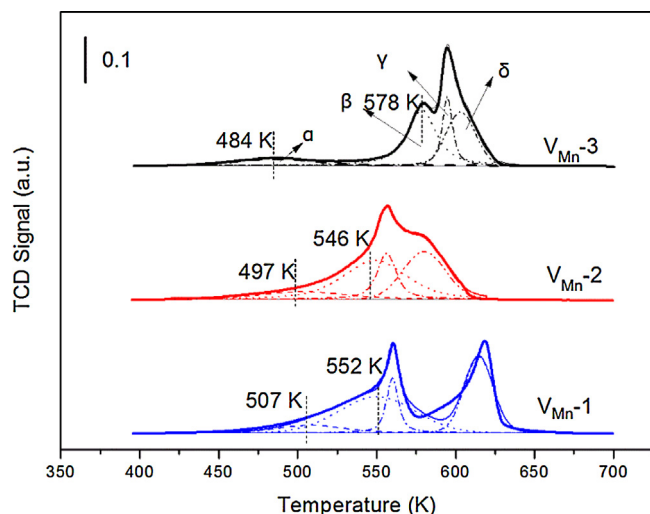


Fig. 7. H₂-TPR profiles of different birnessite samples.

reducible and reactive. This is consistent with the XPS analysis, i.e. the higher content of V_{Mn}, which is compensated by K⁺, the higher ratio of O_{ads}/O_{latt} is. Zhai et al. [46] also reported that alkali ions (K⁺ and Na⁺) promoted surface oxygen and hydroxyl groups associated with atomically dispersed platinum for water-gas shift reactions.

To further learn the function of V_{Mn} during HCHO oxidation process, in-situ DRIFTS spectra were recorded the intermediate species on the surface of catalyst within 60 min for the different birnessite samples at room temperature (Fig. 8). With the exposure time goes, the peaks located at 1562, 1350 and 2840 cm⁻¹ were accumulated over all samples, which can be ascribed to ν_{as}(COO), ν_s(COO) and ν(CH) of formate (HCOO⁻) species [17]. A small peak at 1730 cm⁻¹ appeared on V_{Mn}-3 sample, which can be ascribed

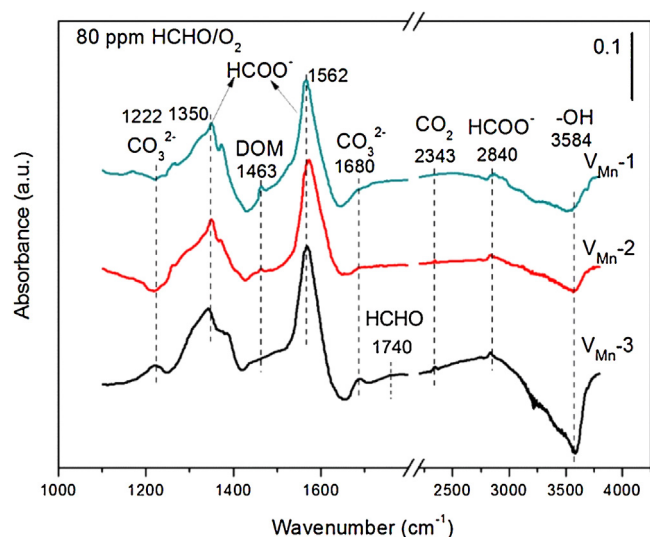


Fig. 8. In-situ DRIFTS spectra of different birnessite samples exposed to the flow of HCHO/O₂ at room temperature.

Table 4

Survey of catalytic performance of manganese oxides in HCHO oxidation.

Catalyst	Reaction conditions	T _{50%} (°C)	Ref.
α-MnO ₂	170 ppm	90	[15]
β-MnO ₂	HCHO,	140	
γ-MnO ₂	GHSV ~ 100000 mL/g	125	
δ-MnO ₂	h	58	
Porous Birnessite	460 ppm HCHO, GHSV ~ 30000 mL/g h	85	[40]
3D-β-MnO ₂	400 ppm	90	[41]
α-MnO ₂	HCHO,	100	
β-MnO ₂	GHSV ~ 30000 mL/g	150	
β-MnO ₂ /SiO ₂	120 ppm HCHO, GHSV ~ 30000 mL/g h	107	[42]
Birnessite	100 ppm	93	[43]
Cryptomelane	HCHO,	85	
Ramsdellite	GHSV ~ 60000 mL/g	100	
MnOOH	h	115	
MnO ₂ /TiO ₂	50 ppm HCHO, GHSV ~ 30000 mL/g h	>60	[44]
Pyrolusite	400 ppm	150	[45]
Cryptomelane	HCHO,	110	
Todorokite	GHSV ~ 18000 mL/g	140	
Birnessite	80 ppm HCHO, GHSV ~ 120000 mL/g h	53	This work

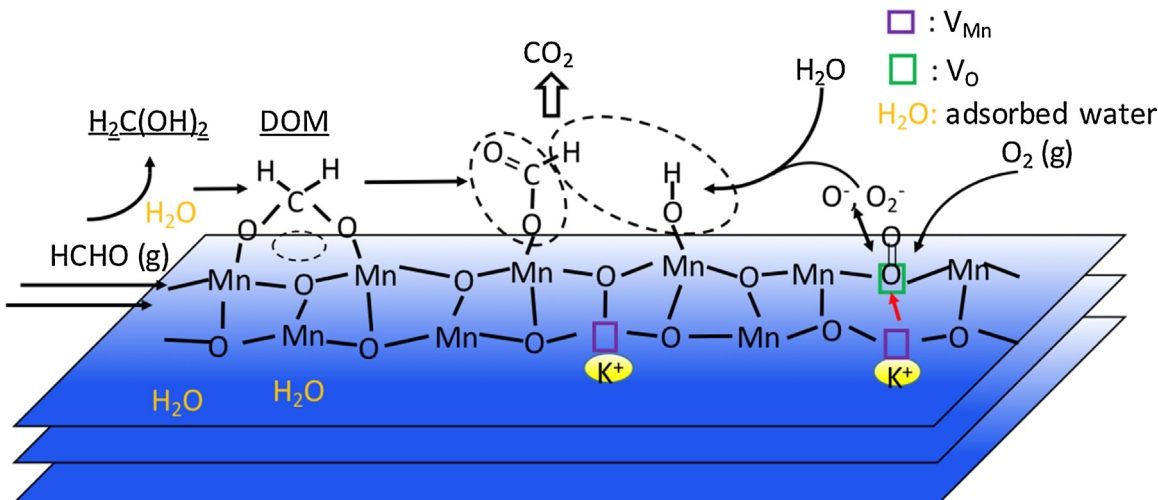


Fig. 9. Reaction pathway of HCHO on layered manganese dioxide with K⁺-compensated manganese vacancies.

to the C=O group of adsorbed HCHO. No obvious peak could be observed on V_{Mn}-1 and V_{Mn}-2 samples, indicating vacancy may be beneficial to the adsorption of HCHO [47]. Formate species were the well-known intermediate during formaldehyde oxidation process. Dioxymethylene (DOM) species ($\delta(\text{CH}_2)$, 1463 cm⁻¹) were also detected over V_{Mn}-1 sample during HCHO oxidation [29,48]. Carbonyl carbon in HCHO is electrophilic, which tends to adsorb on nucleophilic surface oxygen atom and form DOM, which will be further oxidized to formate. With the increase of V_{Mn} content, the peaks of DOM decreased to zero, which indicates that DOM species are more quickly converted to formate with the increase of V_{Mn} content. Besides, there was a negative peak around 3584 cm⁻¹, which can be ascribed to loss of surface hydroxyl groups [6,17]. Surface OH group is a critical species for HCHO oxidation as reported in literatures [6–11]. The negative peak for OH group suggests that the oxidation of HCHO consumed OH groups. In comparison with other two samples, V_{Mn}-3 sample consumed the largest hydroxyl groups during HCHO oxidation, which is consistent with its highest activity for HCHO removal and CO₂ formation as shown in Fig. 7. In addition, the accumulation of carbonate ($\nu_{\text{as}}(\text{COO}^-)$, 1222 cm⁻¹; ($\nu(\text{C=O})$, 1680 cm⁻¹) and CO₂ species (2343 cm⁻¹) were also observed in DRIFTS, confirming that HCOO⁻ was further oxidized into carbonate and CO₂.

The catalytic cycle of HCHO oxidation over birnessite with K⁺-compensated Mn vacancy is summarized in Fig. 9. HCHO is first adsorbed on birnessite, which is enhanced by water contained in birnessite via forming hydrogen bonding with HCHO [17]. Adsorbed HCHO and its hydrate (methanediol, CH₂(OH)₂) would be oxidized by surface active oxygen (O₂⁻, O⁻ or terminal OH group) into DOM, formate, carbonate and CO₂ sequentially. An oxygen vacancy (V_O) will occur after adsorbed oxygen species is consumed for HCHO oxidation. Then dioxygen molecule in air would be adsorbed on V_O and dissociated (O₂ + V_O → O₂⁻, O⁻). The consumed surface OH is replenished via the reaction with H₂O (O₂⁻ + H₂O → 2OH). Thus, the catalytic cycle is finished. Due to the existence of manganese vacancy, potassium ion compensates its charge imbalance, facilitating the formation of surface active oxygen, which in turn acts as the active site for HCHO oxidation.

4. Conclusions

Birnessite samples with different content of manganese vacancies (V_{Mn}) were synthesized via adjusting the reactant ratio of KMnO₄ to (NH₄)₂C₂O₄. It was found that potassium ions increased

with V_{Mn} for the compensation of charge imbalance caused by V_{Mn}. Birnessite samples with higher content of V_{Mn} showed higher ratio of adsorbed oxygen species, which is more reducible and active. As-synthesized samples were tested for HCHO decomposition at room temperature. HCHO is sequentially oxidized to dioxymethylene (DOM), formate and finally to CO₂. The higher the content of manganese vacancy, the better performance for HCHO decomposition and CO₂ generation. This finding sheds light on a way to improve the activity of birnessite for HCHO, i.e. creating more manganese vacancies to increase the content of potassium ions, which will in turn result in more reducible oxygen species for HCHO oxidation.

Acknowledgments

This work was financially supported by Natural Science Foundation (21221004, 21411140032), National Basic Research Program of China (2013CB632403), and Tsinghua University Initiative Scientific Research Program (20131089251).

Appendix A. Supplementary data

Supplementary data associated with this article can be found, in the online version, at <http://dx.doi.org/10.1016/j.apcatb.2016.11.036>.

References

- [1] T. Salhamer, S. Mentese, R. Marutzky, Chem. Rev. 110 (2010) 2536–2572.
- [2] H. Huang, Y. Xu, Q. Feng, D.Y.C. Leung, Catal. Sci. Technol. 5 (2015) 2649–2669.
- [3] J.Q. Torres, S. Royer, J.P. Bellat, J.M. Giraudon, J.F. Lamonier, ChemSusChem 6 (2013) 578–592.
- [4] B. Bai, Q. Qiao, J. Li, J. Hao, Chin. J. Catal. 37 (2016) 102–122.
- [5] L. Nie, J. Yu, M. Jaroniec, F.F. Tao, Catal. Sci. Technol. 6 (2016) 3649–3669.
- [6] C. Zhang, F. Liu, Y. Zhai, H. Ariga, N. Yi, Y. Liu, K. Asakura, M.F. Stephanopoulos, H. He, Angew. Chem. Int. Ed. 51 (2012) 9628–9632.
- [7] L. Nie, J. Yu, X. Li, B. Cheng, Gang. Liu, M. Jaroniec, Environ. Sci. Technol. 47 (2013) 2777–2783.
- [8] H. Huang, X. Ye, H. Huang, L. Zhang, D.Y.C. Leung, Chem. Eng. J. 230 (2013) 73–79.
- [9] C. Zhang, Y. Li, Y. Wang, H. He, Environ. Sci. Technol. 48 (2014) 5816–5822.
- [10] Q. Xu, W. Lei, X. Li, X. Qi, J. Yu, G. Liu, J. Wang, P. Zhang, Environ. Sci. Technol. 48 (2014) 9702–9708.
- [11] B. Bai, J. Li, ACS Catal. 4 (2014) 2753–2762.
- [12] M. Wiechen, I. Zaharieva, H. Dau, P. Kurz, Chem. Sci. 3 (2012) 2330–2339.
- [13] L. Athouël, F. Moser, R. Dugas, O. Crosnier, D. Bélanger, T. Brousse, J. Phys. Chem. C 112 (2008) 7270–7277.
- [14] I. Atribak, A. Bueno-López, A. García-García, P. Navarro, D. Frías, M. Momontes, Appl. Catal. B: Environ. 93 (2010) 267–273.
- [15] J. Zhang, Y. Li, L. Wang, C. Zhang, H. He, Catal. Sci. Technol. 5 (2015) 2305–2313.

- [16] H. Chen, J. He, C. Zhang, H. He, *J. Phys. Chem. C* 111 (2007) 18033–18038.
- [17] J. Wang, P. Zhang, J. Li, C. Jiang, R. Yunus, J. Kim, *Environ. Sci. Technol.* 49 (2015) 12372–12379.
- [18] J. Wang, R. Yunus, J. Li, P. Li, J. Kim, *Appl. Surf. Sci.* 357 (2015) 787–794.
- [19] J. Wang, D. Li, P. Li, P. Zhang, Q. Xu, J. Yu, *RSC Adv.* 5 (2015) 100434–100442.
- [20] H. Wang, J. Zhang, X. Hang, X. Zhang, J. Xie, B. Pan, Y. Xie, *Angew. Chem.* 127 (2015) 1211–1215.
- [21] J. Yan, G. Wu, N. Guan, L. Li, Z. Li, X. Cao, *Phys. Chem. Chem. Phys.* 15 (2013) 10978–10988.
- [22] X. Liu, K. Zhou, L. Wang, B. Wang, Y. Li, *J. Am. Chem. Soc.* 131 (2009) 3140–3141.
- [23] A. Janotti, J.B. Varley, P. Rinke, N. Umezawa, G. Kresse, C.G. Van de walle, *Phys. Rev. B* 81 (2010) 085212.
- [24] L. Zeng, W. Song, M. Li, D. Zeng, C. Xie, *Appl. Catal. B: Environ.* 147 (2014) 490–498.
- [25] Y. Wang, X. Feng, M. Villalobos, W. Tan, F. Liu, *Chem. Geol.* 292 (2012) 25–34.
- [26] W. Zhao, H. Cui, F. Liu, W. Tan, X. Feng, *Clay Clay Miner.* 57 (2009) 513–520.
- [27] K.D. Kwon, K. Refson, G. Sposito, *Geochim. Cosmochim. Acta* 73 (2009) 4142–4150.
- [28] K.D. Kwon, K. Refson, G. Sposito, *Phys. Rev. Lett.* 100 (2008) 146601.
- [29] S.J. Park, I. Bae, I.S. Nam, B.K. Cho, S.M. Jung, J.H. Lee, *Chem. Eng. J.* 195 (2012) 392–402.
- [30] J.H. Lee, R. Black, G. Popov, E. Pomerantseva, F. Nan, G.A. Botton, L.F. Nazar, *Energy Environ. Sci.* 5 (2012) 9558–9565.
- [31] Z. Liu, R. Ma, Y. Ebina, K. Takada, T. Sasaki, *Chem. Mater.* 19 (2007) 6504–6512.
- [32] K. Frey, V. Iablokov, G. Sáfrán, J. Osánd, I. Sajóe, R. Szukiewicza, S. Chenakina, N. Krusea, *J. Catal.* 287 (2012) 30–36.
- [33] E.J. Silvester, M. Drifts, *Am. Miner.* 82 (1997) 962–978.
- [34] A.C. Gaillot, D. Flot, V.A. Drifts, A. Manceau, M. Burghammer, B. Lanson, *Chem. Mater.* 15 (2003) 4666–4678.
- [35] T. Mathew, K. Suzuki, Y. Ikuta, N. Takahashi, H. Shinjoh, *Chem. Commun.* 48 (2012) 10987–10989.
- [36] M. Setvín, U. Aschauer, P. Scheiber, Y.F. Li, W. Hou, M. Schmid, A. Selloni, U. Diebold, *Science* 341 (2013) 988–991.
- [37] G.I. Panov, K.A. Dubkov, E.V. Starokon, *Catal. Today* 117 (2006) 148–155.
- [38] Q. Fu, H. Saltsburg, M.H. Stephanopoulos, *Science* 301 (2003) 935–938.
- [39] B. Qiao, A. Wang, X. Yang, L.F. Allard, Z. Jiang, Y. Cui, J. Liu, J. Li, T. Zhang, *Nat. Chem.* 3 (2011) 634–641.
- [40] H. Tian, J. He, L. Liu, D. Wang, Z. Hao, C. Ma, *Microporous Mesoporous Mater.* 151 (2012) 397–402.
- [41] B. Bai, Q. Qiao, J. Li, J. Hao, *Chin. J. Catal.* 37 (2016) 27–31.
- [42] R. Averlant, S. Royer, J.M. Giraudon, J.P. Bellat, I. Bezverkhyy, G. Weber, J.F. Lamontier, *ChemCatChem* 6 (2014) 152–161.
- [43] L. Zhou, J. Zhang, J. He, Y. Hu, H. Tian, *Mater. Res. Bull.* 46 (2011) 1714–1722.
- [44] T. Yang, Y. Huo, Y. Liu, Z. Rui, H. Ji, *Appl. Catal. B: Environ.* 200 (2017) 543–551.
- [45] T. Chen, H. Dou, X. Li, X. Tang, J. Li, J. Hao, *Microporous Mesoporous Mater.* 122 (2009) 270–274.
- [46] Y. Zhai, D. Pierre, R. Si, W. Deng, P. Ferrin, A. Nilekar, G. Peng, J.A. Herron, D.C. Bell, H. Saltsburg, M. Mavrikakis, M. Flytzani-Stephanopoulos, *Science* 329 (2010) 1633–1636.
- [47] H. Chen, M. Tang, Z. Rui, H. Ji, *Ind. Eng. Chem. Res.* 54 (2015) 8900–8907.
- [48] D. Chen, Z. Qu, Y. Sun, K. Gao, Y. Wang, *Appl. Catal. B: Environ.* 142 (2013) 838–848.